Materials Advances

ROYAL SOCIETY OF CHEMISTRY

PAPER

View Article Online
View Journal | View Issue

Cite this: *Mater. Adv.*, 2021, **2**, 1665

Photo-energy conversion efficiency of $CH_3NH_3PbI_3/C_{60}$ heterojunction perovskite solar cells from first-principles†

Khian-Hooi Chew, *[a] Riichi Kuwahara [b] and Kaoru Ohno [c]

Halide perovskites have emerged as the most potential candidate for the next-generation solar cells. In this work, we conduct a comprehensive first-principles study on the photo-energy conversion efficiency (PCE) of the $CH_3NH_3PbI_3/C_{60}$ heterojunction. Since perovskite solar cells (PSCs) are generally exposed to substantial temperature variations that affect the photo-physics and charge separation in the perovskites, finite slabs of both the tetragonal- and cubic-phases of $CH_3NH_3PbI_3$ ($MAPbI_3$) are constructed with different orientations of the methylammonium (MA) cation with respect to the perovskite surface. A C_{60} molecule, acting as an electron acceptor and transport material, is introduced at various positions on the $MAPbI_3$ surface. Using the detailed balance approach, the PCE of the heterojunction is determined by examining the Kohn–Sham energies and orbitals located either in $MAPbI_3$ or in C_{60}. Our study reveals that the stability, the exciton dissociation efficiency, and the PCE of the tetragonal $MAPbI_3/C_{60}$ heterojunctions strongly depend on the MA orientation and the C_{60} position on the $MAPbI_3$ surface. This is attributed to the polar behavior of $MAPbI_3$. Using the tetragonal-phase heterojunction, a high PCE of $\eta \sim 19\%$ can be achieved, if certain surface conditions are met. Built-in electric field originating from the surface dipoles of the MA cation facilitates the dissociation of electron–hole pairs and the electron transfer to fullerene. On the other hand, the heterojunction with a high-temperature cubic $MAPbI_3$ structure exhibits a PCE of $\eta \sim 10\%$, regardless of the MA orientation and C_{60} on the $MAPbI_3$ surface.

Received 1st November 2020,
Accepted 25th December 2020

DOI: 10.1039/d0ma00853b

rsc.li/materials-advances

1 Introduction

Halide perovskites are considered to be the most promising materials for the next generation of photovoltaics.[1] This is because of their low cost and high energy conversion efficiency achieved within a relatively short period of research and development. The photo-energy conversion efficiency (PCE) of perovskite solar cells (PSCs) made of $CH_3NH_3PbI_3$ (hereafter, it is denoted as $MAPbI_3$, where MA means methylammonium CH_3NH_3) and its derivatives have increased from 3.8% to over 20% in recent years.[2–5] Among the factors that contribute to the high performance of PSCs are inert interface defects,[6] reduced bimolecular recombination,[7] a long charge carrier lifetime,[8] and low densities of the conduction and valence band states.[9] $MAPbI_3$ undergoes several structural transitions; a cubic phase at temperature above 330 K, a tetragonal phase at temperature between 160 K and 330 K, and an orthorhombic phase at temperature below 160K.[10] Thus, the orthorhombic phase is not a stable structure at room temperature. Generally, solar cells are exposed to a wide range of temperatures. The actual operating temperature inside a solar cell can be much higher than the ambient temperature due to the heating from the solar irradiation.[11] Therefore, it is important to explore the fundamental photovoltaic properties of both the cubic and tetragonal phases.

Fullerenes, in particular C_{60}, have been employed in organic solar cells as acceptors for over two decades,[12–16] and there is increasing interest in the application of fullerenes to PSCs.[13–16] It has been demonstrated that fullerenes can effectively passivate the charge trap states at surfaces and grain boundaries of perovskites, leading to the suppression of hysteresis and the enhancement of efficiency in PSCs.[21,22] Fullerenes were initially introduced into PSCs as an electron-transport layer with an efficiency of ~3.9% by Jen *et al.*[23] Since the introduction of fullerenes into PSCs, the PCE has been reported to be increased up to over 20%.[24] Many studies indicate that a sufficient

[a] *Department of Physics, University of Malaya, 50603 Kuala Lumpur, Malaysia. E-mail: khchew@um.edu.my*
[b] *Dassault Systèmes, ThinkPark Tower, 2-1-1 Osaki, Shinagawa-ku, Tokyo 141-6020, Japan*
[c] *Department of Physics, Yokohama National University, 79-5 Tokiwadai, Hogogaya-ku, Yokohama 240-8501, Japan*

† Electronic supplementary information (ESI) available. See DOI: 10.1039/d0ma00853b

thickness of fullerenes is important to effectively extract electrons from perovskites.[25–27] However, Liu *et al.* recently reported that an ultrathin fullerene layer of only 1 nm is sufficient to achieve a good performance of PSCs.[28] They also showed that the removal of the fullerene layer leads to a dramatic reduction in the efficiency of the PSCs. It is obvious that a full understanding of mechanisms underlying the interactions at their interface is crucial to improve the efficiency.

A typical PSC comprises of the perovskite as a photo-absorber sandwiched between two electrodes. An interface layer is introduced between the photo-absorber and electrodes to facilitate the charge transport process. The interface layer can be either an n-type electron transport material (ETM) or a p-type hole transport material (HTM). Most of the state-of-the-art PSCs have a transparent conducting oxide/ETM/Perovskite/HTM/metal architecture. Typical HTMs are Spiro-MeOTAD, or PEDOT:PSS, while the typical ETMs include C_{60} or PCBM.[1,17–20] Understanding the interaction at interfaces and optimizing the energy alignments offer a very exciting area of research that is still under discussion.[1,17–20] Despite the PCE of over 20%[5] has been achieved, the low long-term stability under moisture[29] or thermal[30] stress stands as their serious drawback. In addition, point defects were reported as another source of degradation because of their high affinity for water and oxygen molecules.[31] The application of Spiro-MeOTAD as HTMs in PSCs[3,32] has made an important step in improving the device performance, however, the PSCs with HTM suffer from degradation.[33–35] Etgar *et al.*[36] demonstrated that perovskite $MAPbI_3$ can function as both a photo-absorber and a hole transporter, suggesting HTM-free PSCs.[1,37] Recently, Wu *et al.* reported HTM-free PSCs with a more simple structure of ITO/$MAPbI_3$/ETM/Cu with 2,3,5,6-tetrafluoro-7,7,8,8-tetracyanoquinodimethane (F4TCNQ) molecules as electron acceptors, which showed a PCE of over 20%.[38] Though the study of HTM-free PSCs is lagging behind of PSCs with HTM, the HTM-free PSC emerges as an alternative option to avoid the degradation problem related to the HTM.

Atomistic modelling and simulation based on first-principles density functional theory (DFT) can play an important role in revealing the underlying mechanisms of the high performance of PSCs.[39–41] Yin *et al.* studied the energy alignment and charge transfer properties at the interface between $MAPbI_3$ perovskites and hole acceptor Spiro-MeOTAD and electron acceptor PCBM.[42] They found that the $MAPbI_3$(001) and (110) surfaces favor hole injection to the hole acceptor Spiro-MeOTAD, whereas the polar $MAPbI_3$(001) surface facilitates electron transfer to the PCBM. Quarti *et al.*[43] investigated the effect of surface termination on the energy level alignment at the interface between C_{60} fullerene and the $MAPbI_3$ perovskite. For the PbI-terminated surface of $MAPbI_3$, the conduction band edge (CBE) of the $MAPbI_3$ perovskite lies below the lowest unoccupied molecular orbital (LUMO) of the C_{60} fullerene, prohibiting the injection of electrons from $MAPbI_3$ into C_{60}. On the other hand, the CBE of the MAI-terminated perovskite located above the LUMO of C_{60}, favoring the electron transfer into C_{60}. The highest occupied molecular orbital (HOMO) of the C_{60} fullerene is always located below the valence band edge (VBE) of the $MAPbI_3$ perovskite. Hereafter, we also call the CBE and VBE of $MAPbI_3$ perovskite as the LUMO and HOMO of the $MAPbI_3$ perovskite in order to simplify the discussion. As well, the energy levels of the whole system are denoted as HOMO−1, HOMO, LUMO, LUMO+1, LUMO+2,... irrespective of the location of the orbitals.

Numerous experimental and theoretical studies have been devoted to $MAPbI_3/C_{60}$ heterojunction PSCs. However, the efficiency of the exciton formation and dissociation in heterojunction interfaces between the donor ($MAPbI_3$) and acceptor (C_{60}) remains unclear. This motivates the present study to develop a comprehensive understanding of the PCE of $MAPbI_3/C_{60}$ heterojunctions for both the tetragonal and cubic $MAPbI_3$. In this study, finite $MAPbI_3$ slabs are constructed with different orientations of the MA cation with respect to the surface. A C_{60} molecule is introduced to various positions on the $MAPbI_3$ surface. A systematic study on how the MA orientation and the C_{60} position on the $MAPbI_3$ surface influence the stability, the exciton dissociation efficiency, and the PCE of $MAPbI_3/C_{60}$ heterojunctions is performed in detail using first-principles density functional theory (DFT). The PCE of the heterojunctions is estimated by using the detailed balance approach.[44–46]

2 Model for perovskite solar cells

We consider a HTM-free PSC consisting of a heterojunction of perovskite $MAPbI_3$ and fullerene C_{60}, as shown in Fig. 1.

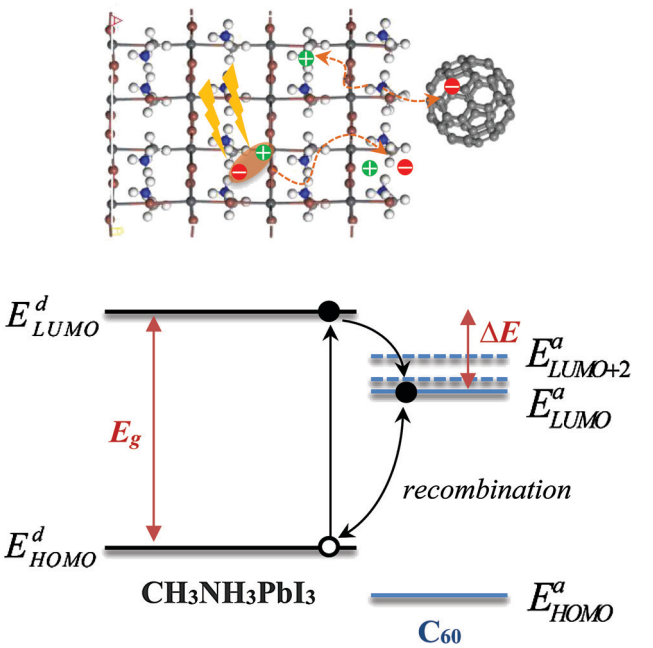

Fig. 1 Schematic illustration of the energy-level diagram for the $MAPbI_3$ and C_{60} in the hybrid perovskite/fullerene heterojunction. E_g is the energy gap of $MAPbI_3$ and ΔE is the dissociation energy of the electron–hole pairs. The three-fold degenerate LUMO of C_{60} fullerene has three energy levels from the LUMO to LUMO+2.

A schematic energy diagram of the heterojunction of a $MAPbI_3$ and C_{60} solar cell is also illustrated in Fig. 1. The perovskite donor absorbs a photon of energy $E_g = E^d_{LUMO} - E^d_{HOMO}$ to excite electrons from the HOMO to the LUMO, leaving holes behind in the perovskite, which also function as HTM. Here, E^d_{LUMO} and E^d_{HOMO} denote the energy eigenvalues of the LUMO and HOMO of the $MAPbI_3$ donor, respectively. The photogenerated electrons with the energy E^d_{HOMO} move to the lower energy E^a_{LUMO} level of acceptor C_{60}. The energy loss associated with the transition of electrons from the donor $MAPbI_3$ to acceptor C_{60} is given by $\Delta E = E^d_{LUMO} - E^a_{LUMO}$. Some of these electrons may recombine with the holes, which was not considered in the Shockley–Queisser (SQ) limit.[44]

Using the detailed balance model as proposed by Seki *et al.*,[45] we calculate the photo-energy conversion efficiency (PCE) η of the $MAPbI_3/C_{60}$ heterojunction solar cell for various MAI terminations of the $MAPbI_3$ perovskite. The magnitude of $\eta(E_g, \Delta E)$ is defined by the ratio of the maximum electric power to the radiative power irradiated at a solar cell as follows

$$\eta(E_g, \Delta E) = \frac{\mathrm{Max}\{eV[J_p(E_g) - J_r(E_g - \Delta E, V)]\}_V}{\int_0^\infty E j_p(E) dE}, \quad (1)$$

where e is the electron charge and V is the photo-voltage. $\int_0^\infty E j_p(E) dE$ describes the radiative power input. In eqn (1), the photon flux per unit area entering the solar cell $J_p(E_g)$ is given using

$$J_p(E_g) = \int_{E_g}^\infty j_p(E) dE, \quad (2)$$

where $j_p(E)$ denotes the input radiative power, which can be obtained using the air mass 1.5 global (AM1.5G) solar spectrum.[47] On the other hand, the photon flux per unit area by the radiative recombination of charge carriers is

$$J_r(E_g - \Delta E, V) = \exp\left(\frac{eV}{k_B T}\right) \int_{E_g - \Delta E}^\infty j_b(E) dE, \quad (3)$$

where k_B, T, and $j_b(E)$ represent the Boltzmann constant, the temperature of the solar cell, and the black-body radiation spectrum, respectively. The values of E_g and ΔE can be obtained by examining the spatial distribution of the Kohn–Sham (KS) orbitals at the $MAPbI_3/C_{60}$ interface based on the first-principles method, which will be presented in the following section.

3 Computational methods

First-principles calculations were performed using DFT implemented in the DMol^3 package.[48,49] DMol^3 adopts the basis set of numerical atomic orbitals that are the exact solutions to the KS equations for the isolated atoms.[50] A standard KS DFT Dispersion (DFT-D) correction was employed for the corrective calculation of van der Waals dispersion.[51] The van der Waals interaction was included by taking into account the Tkatchenko-Scheffler (TS) scheme.[52,53] In the present study, we considered a slab model of tetragonal phase of $MAPbI_3$(001) with MAI-terminated surfaces. The slab model has a 2 × 2 periodicity in-plane and four MAI-layer thickness. A 50 Å vacuum region between the slabs is adopted, which is rather large enough to avoid the interaction between periodic images. The $MAPbI_3$ slab model and C_{60} fullerene were first optimized to achieve the minimum energy. We introduced one C_{60} fullerene molecule on the $MAPbI_3$(001) layer, forming a hybrid $MAPbI_3/C_{60}$ structure with a total of 444 atoms (see Fig. 1). For the perovskite/fullerene interface, the dipole slab correction for the electrostatic potential was taken into account in the calculations due to the existence of polar bonds.

All calculations were performed based on the spin restricted approach using the generalized gradient approximation (GGA), in the form of the Perdew–Burke–Ernzerhof (PBE) approximation to the exchange–correlation functional.[54] As the calculations involve a large number of atoms, the spin–orbit coupling (SOC) effect is not included because the PBE functional can provide reasonable estimation on structural, electronic and optical properties.[55–57] In the present study, the GGA-PBE calculations are justified as an approximation to the time-dependent DFT for studying the optically excited states. In particular, the small energy gap, *i.e.*, the deeper LUMO energy, can be regarded as a result of the exciton formation.[16] The double-numerical quality basis set, the Double Numerical plus Polarization (DNP) functions, was employed for all calculations. The size of the DNP basis set is comparable to that of the Gaussian 6-31G**. Due to the presence of hydrogen atoms, the all-electron relativistic method was adopted in the calculations. In the calculations, the geometrical optimization was performed with a Fermi smearing of 0.005 Hartree. The tolerances of the energy, gradient, and displacement convergences were set at 1×10^{-5} Ha, 2×10^{-3} Ha Å^{-1} and 5×10^{-3} Å, respectively.

4 Results and discussion

A PSC has a general structure of oxide/ETM/Perovskite/HTM/metal with one boundary being the ETM/$MAPbI_3$ interface, while the other interface is $MAPbI_3$/HTM. In other words, the perovskite film has asymmetric boundaries in nature. Therefore, we consider an asymmetric slab model with the MAI as the top surface layer (facing the upper vacuum) and the PbI layer as the bottom layer of $MAPbI_3$ (facing the lower vacuum). Here, the MAI-terminated surface is set as the $MAPbI_3$ top surface because this surface facilitates the electron transfer to the C_{60} ETM.[40] We consider both the tetragonal and cubic perovskite $MAPbI_3$, which we denote as the "*t*-MAI" and "*c*-MAI" slab models, respectively.

The finite slab models are constructed with three different orientations of the MA cation with respect to the top surface (as shown in Fig. 2): (i) the apolar model, in which half of the MA cations have their $-NH_3$ or $-CH_3$ groups pointing upward (and half pointing downward), (ii) the topC model, in which the CH_3 group of MA cations orients towards the upper vacuum in all layers, and (iii) the topN model, in which the NH_3 group of the MA cation aligns towards the upper vacuum in all layers.

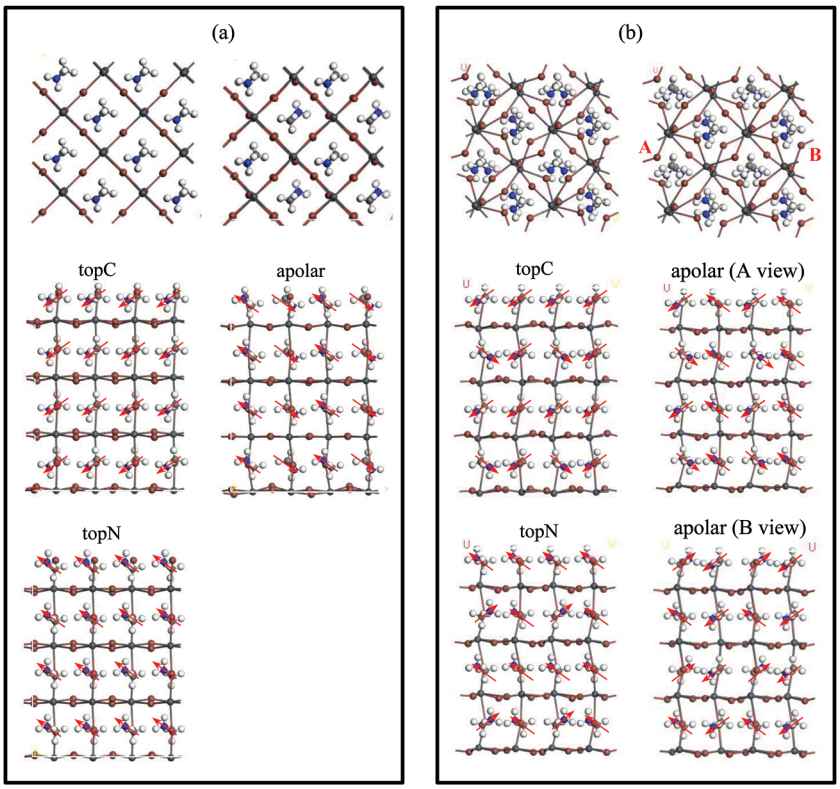

Fig. 2 Top and side views of (a) cubic and (b) tetragonal $MAPbI_3$(001) surfaces with MAI terminations for topC, topN and apolar geometries. Two different side views (from A and B sides) of the tetragonal $MAPbI_3$(001) surface are shown for clarity. H, C, N, I, and Pb atoms are represented by the white, light grey, blue, brown, and dark grey spheres, respectively. Red arrow represents the molecular dipole of a MA cation with the NH_3 group as the arrow head.

The computationally optimized cell parameters for the bulk tetragonal phase of $MAPbI_3$ are a = 8.695 Å, b = 8.715 Å and c = 12.835 Å, while $a = b = c$ = 6.351 Å for the cubic phase. The cubic $MAPbI_3$ structure employed in this study is a ferroelectric phase, in which the MA cations align along the [100] direction, instead of MA cations with random orientations as reported in experiments.[58,59] This cubic phase is just a model structure, although the calculated lattice constants agree well with the experiments.[60,61] The calculated cell parameters for the bulk tetragonal structure are comparable to the experimental values.[10,60]

4.1 $MAPbI_3$ surfaces

We first look at the energetics of the finite slab models. Since the main focus of this study is on the PCE of $MAPbI_3/C_{60}$ heterojunctions, a detailed study on the structural phenomena is beyond the scope of the present study. Therefore, we will not present the structural phenomena related to surface reconstructions. In Table 1, we summarize the valence band edge (VBE), conduction band edge (CBE), band gap, and the total relative energies of the *c*-MAI and the *t*-MAI models for perovskites with the bare surface. Generally, the *t*-MAI model

Table 1 Calculated valence band edge VBE, conductance band edge CBE, band gap, total DFT-D energy and the relative energies of the $MAPbI_3$ slab models for different MAI orientations

Structure (model)	Surface geometry	VBE [eV]	CBE [eV]	Band gap [eV]	Total DFT-D energy [eV]	Total energy relative to the topC (*t*-MAI) [eV]
Cubic (c-MAI)	TopC	−5.412	−3.683	1.729	−33296273.965	3.550
	TopN	−4.682	−3.763	0.919	−33296271.732	5.783
	Apolar	−5.114	−3.705	1.409	−33296272.945	4.570
	Other works			1.38[a], 1.51[b]		
	Expt.			1.61[c]		
Tetragonal (*t*-MAI)	topC	−5.398	−3.912	1.486	−33296277.515	0.000
	topN	−4.657	−3.582	1.075	−33296273.703	3.812
	apolar	−4.917	−3.645	1.272	−33296275.013	2.502
	Other works			1.60[d]		
	Expt.			1.55[e]		

[a] Ref. 62. [b] Ref. 63. [c] Ref. 64. [d] Ref. 42. [e] Ref. 65.

with tetragonal structures (relative energies range from 0.0 to ~3.8 eV) is more stable than the *c*-MAI with cubic structures (relative energies range from ~3.6 to ~5.8 eV). Among them, the *t*-MAI model with the topC orientation is the most stable structure with a bandgap of 1.486 eV in agreement with other studies.[42,66] The predicted bandgap of ~1.73 eV for the *c*-MAI model with the topC orientation is comparable to the experimental value of 1.61 eV.[64] The calculated VBE and CBE for the *t*-MAI model phases are −4.66 to −5.40 eV and −3.58 to −3.91 eV, respectively. For the *c*-MAI model, the calculated VBEs range from −4.68 to −5.41 eV and the CBE ranges from −3.68 to −3.76 eV. Note that although the GGA-PBE calculations usually underestimate the bandgap of semiconductors, the agreements are due to the fortuitous cancellation of the GGA underestimated gap and the excluding of the spin-order interaction, which tends to overestimate the gap.[66]

4.2 $MAPbI_3/C_{60}$ heterojunctions

We now examine the PCE of the $MAPbI_3/C_{60}$ heterojunctions. Using the *t*-MAI and *c*-MAI slab models, we introduce one C_{60} molecule on several positions on the $MAPbI_3$ surface, as shown in Fig. 3. We then perform a structural optimization of the various models, and identify the energy levels of the $MAPbI_3$ and C_{60} by examining the KS orbitals. Then, the energy levels of the acceptor C_{60} LUMO (E^{a}_{LUMO}) and the donor $MAPbI_3$ HOMO/LUMO ($E^{d}_{HOMO}/E^{d}_{LUMO}$) are found by the KS energy eigenvalues. Then, the PCE (η) of the $MAPbI_3/C_{60}$ heterojunction solar cell is obtained by determining the HOMO–LUMO gap of $MAPbI_3$ $E_g = E^{d}_{LUMO} - E^{d}_{HOMO}$ and the electron–hole pair dissociation energy $\Delta E = E^{d}_{LUMO} - E^{a}_{LUMO}$.

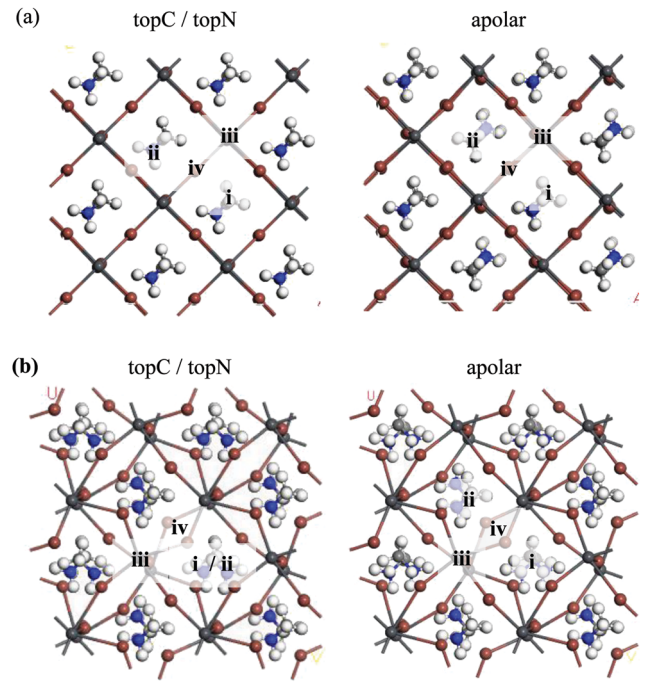

Fig. 3 Position of a fullerene C_{60} on (a) cubic and (b) tetragonal $MAPbI_3$(001) surfaces with MAI terminations for topC/topN and apolar geometries: (i) aboveC, (ii) aboveN, (iii) aboveI, and (iv) bridge. H, C, N, I, and Pb atoms are represented by the white, light grey, blue, brown, and dark grey spheres, respectively. H, C, N, I, and Pb atoms are represented by the white, light grey, blue, brown, and dark grey spheres, respectively.

4.2.1 Kohn–Sham (KS) orbitals and energy eigenvalues. We first investigate the $MAPbI_3/C_{60}$ heterojunction with tetragonal-phase perovskites based on the *t*-MAI slab models. The optimized structures of the tetragonal-phase heterojunctions with a topC, topN, and apolar geometries are illustrated in Fig. S1–S3 (see the ESI†). In Fig. 4, we show the spatial distribution of the KS orbitals from the HOMO−1 to LUMO+3 of a $MAPbI_3/C_{60}$ heterojunction for the topC geometry with C_{60} at the aboveC, aboveI, and apolar positions. In general, the HOMO−1 and LUMO+3 mainly localized in $MAPbI_3$ though some orbitals can be found in the C_{60} molecule. On the other hand, the orbitals of the LUMO+1 and LUMO+2 are not strictly localized in the fullerene C_{60} molecule, but expand to the first and second layers of $MAPbI_3$. Here, the highest and lowest occupied molecular orbitals of $MAPbI_3$ are denoted by the HOMO and LUMO+3, respectively. The LUMO, LUMO+1, and LUMO+2 are the three energy levels of the (originally three-fold degenerate) LUMO of C_{60}, as shown in Fig. 4. An interesting feature, which can be observed from the spatial distribution of the KS orbital is that the HOMO of a heterojunction with C_{60} at the aboveC position on a topC orientation is located not only in the C_{60} molecule, but also in the top to the bottom (whole) layers of $MAPbI_3$. For the case of a topN heterojunction (see Fig. S7 in the ESI†) with C_{60} at the aboveI or bridge position, the KS orbitals of the HOMO level can be found only in the bottom layer of $MAPbI_3$. The KS orbitals of the $MAPbI_3/C_{60}$ heterojunctions with the apolar geometry have a similar spatial distribution to the case with the topN geometry, as shown in Fig. S8 (ESI†). However, there is a distinct difference between Fig. 4 (topC geometry) and Fig. S7 and S8 (ESI†) (topN & apolar geometries) in the KS wave function at the HOMO and HOMO−1 levels. The former has enough amplitude in the upper perovskite surface and even in C_{60} but the latter has almost no amplitude in the upper perovskite surface and C_{60}. From this comparison, we find that the topC surface is compatible with C_{60} but the topN surface is incompatible with C_{60}. This is clear evidence of the symmetry breakdown due to the asymmetry of the MA molecule. Due to this effect, topC geometry has a deeper HOMO energy compared with the other geometries. In the same reason, the topC geometry has a deeper energy of the LUMO+3 level (*i.e.*, the CBE of $MAPbI_3$), which results in a relatively higher photo-energy conversion efficiency (PCE). The PCE of the PSCs will be discussed later.

Optimized structures of the cubic-phase heterojunctions for different surface geometries are shown in Fig. S9–S11 (in the ESI†). For the case of cubic-phase heterojunction, the topC case with C_{60} on the aboveI position could not converge during geometrical optimization. Therefore, we only discuss the topC case with C_{60} on the aboveC and apolar positions. The KS orbitals from the HOMO−1 to LUMO+3 of a cubic-phase $MAPbI_3/C_{60}$ heterojunction for various surface geometries are shown in Fig. S9–S11 (ESI†). In general, the KS orbitals of the cubic-phase heterojunction exhibit behaviors similar to those

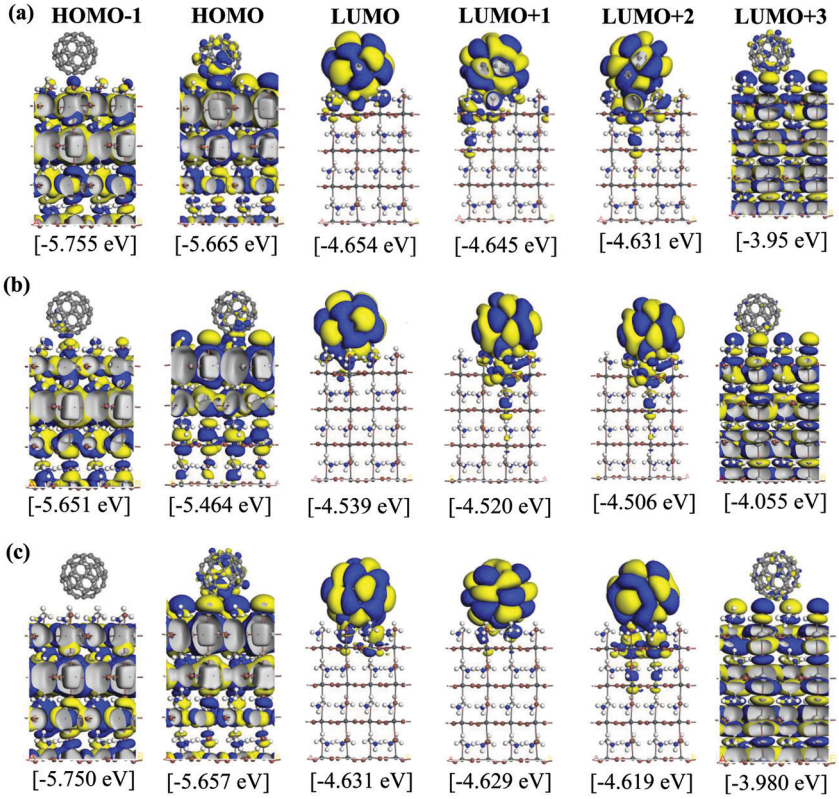

Fig. 4 Calculated Kohn–Sham orbitals and energy eigenvalues of a $MAPbI_3/C_{60}$ heterojunction with tetragonal $MAPbI_3$ from HOMO−1 to LUMO+3 levels. Yellow and blue denote plus and minus regions of the orbitals. The perovskite has a topC geometry with a fullerene C_{60} on the (a) aboveC, (b) abovel and (c) bridge positions.

of the heterojunction with tetragonal-phase structures. For the case of the topN and apolar geometries, it is interesting to see that some orbitals of the HOMO and HOMO−1 are located at lower layers only. Similar to the case of tetragonal-phase heterojunctions, the orbitals of the LUMO+1 and LUMO+2 are located not only in C_{60}, but also in the first and second layers of $MAPbI_3$.

4.2.2 Structural stabilities and binding energies of $MAPbI_3/C_{60}$ PSCs. Stability of $MAPbI_3$ structures is important for achieving efficient PSCs. Fig. 5(a) illustrates the total DFT-D energies of a $MAPbI_3/C_{60}$ heterojunction relative to the topC-aboveC configuration. The corresponding numerical values are summarized in Table S1 (ESI†). As seen from Fig. 5(a), the most stable bare $MAPbI_3$ surface is the tetragonal perovskite with the topC orientation. The next stable finite $MAPbI_3$ slab with the bare surface is the tetragonal perovskite with the apolar orientation. The instability for the finite $MAPbI_3$ slab with the bare surface for the tetragonal $MAPbI_3$ increases as *t*-MAI & topC > *t*-MAI & apolar > *t*-MAI & topN, while it increases as *c*-MAI & topC > *c*-MAI & apolar > *c*-MAI & topN for the cubic $MAPbI_3$. From Fig. 5(a), it is seen that the order of stability remains the same as the bare $MAPbI_3$ surface of tetragonal $MAPbI_3$, regardless of the adsorption position of C_{60} on the tetragonal $MAPbI_3$ surface. The introduction of C_{60} on the cubic $MAPbI_3$ surface, however, shows an unexpected energetic behavior. In particular, the total energy of $MAPbI_3/C_{60}$ heterojunctions with cubic $MAPbI_3$ does not show any obvious dependence on the MA orientation, as well as on the adsorption position of C_{60} on the cubic $MAPbI_3$ surface.

In Fig. 5(b), we show the calculated binding energy of the $MAPbI_3/C_{60}$ heterojunction and the corresponding numerical values are listed in Table S4 (ESI†). The basis set superposition error (BSSE) was not considered in the calculations because the Dmol^3 code can only implement the BSSE calculations on an isolated system. On the other hand, it is widely accepted that the BSSE effect is minimized and can be neglected when the numerical basis set is used.[48,49] In addition, Inada and Orita confirmed that the numerical basis set implemented in DMol^3 is very small in comparison with the Gaussian basis set.[67] This is because the DMol^3 code adopts exact DFT spherical-atomic orbitals, which are generated numerically. The binding energy E_b is defined as $E_b = E(MAPbI_3/C_{60}) - E(MAPbI_3) - E(C_{60})$, where $E(MAPbI_3/C_{60})$, $E(MAPbI_3)$ and $E(C_{60})$ are the total energies for the heterojunction, $MAPbI_3$ and isolated C_{60}. Generally, the binding energies of $MAPbI_3/C_{60}$ PSCs with cubic $MAPbI_3$ are stronger than that of the heterojunction with the tetragonal structure. For both the cubic and tetragonal $MAPbI_3$, the binding energies do not strongly depend on the adsorption position of C_{60} on the $MAPbI_3$ surface. Both the cubic and tetragonal $MAPbI_3$ have the binding trend of topN > apolar > topC.

4.2.3 Electron–hole pair dissociation energy and photo-energy conversion efficiency. In order to gain insight into the

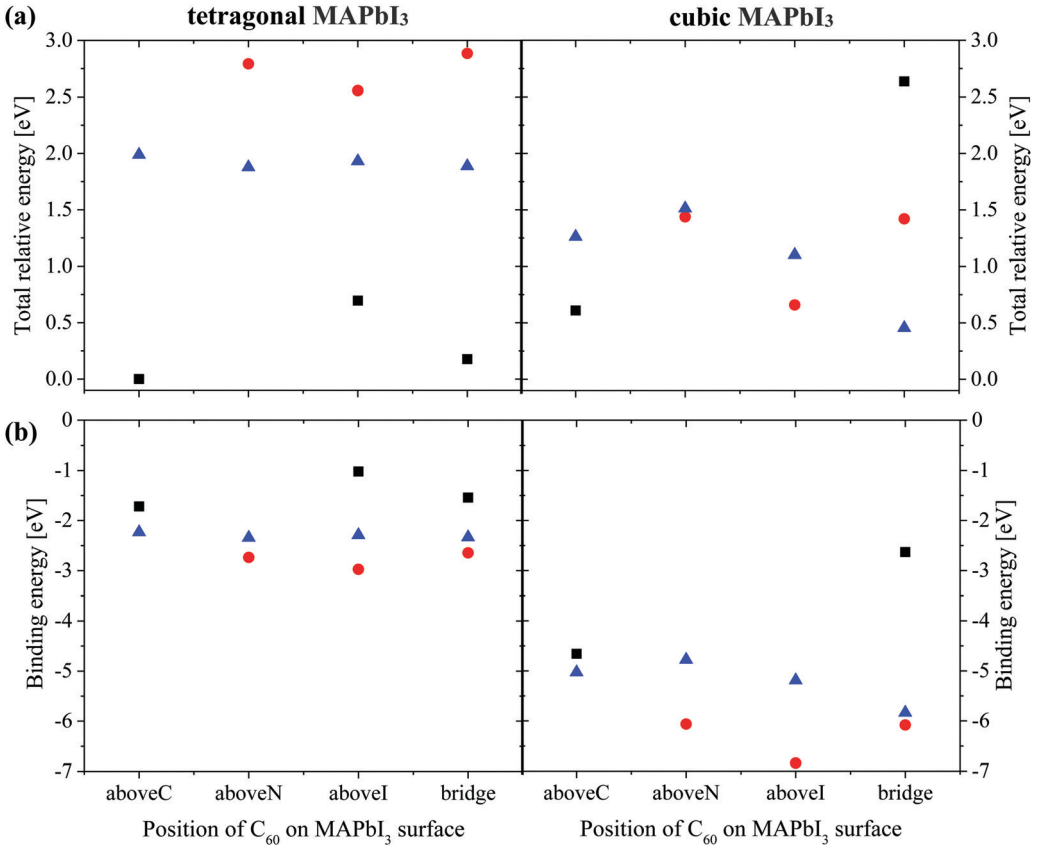

Fig. 5 (a) Total DFT-D and (b) binding energies of a $MAPbI_3/C_{60}$ heterojunction relative to the topC-aboveC configuration. Orientations of the MA cation with respect to the (001) surface are: topC (black), topN (red) and apolar (blue).

charge separation mechanism of $MAPbI_3/C_{60}$ heterojunctions, we examine the energy gap, exciton dissociation energies, and the PCEs, as shown in Fig. 6. The calculated energy gap E_g, the dissociated energy of the electron–hole pair ΔE, and the PCE η of a $MAPbI_3/C_{60}$ heterojunction with tetragonal and cubic $MAPbI_3$ are summarized in Tables S2 and S3 (ESI†), respectively. Fig. 6 provides a comparative relationship of the energy gap of $MAPbI_3$, the exciton dissociation energy, and the PCE of $MAPbI_3/C_{60}$ heterojunctions between tetragonal and cubic $MAPbI_3$. In general, the $MAPbI_3/C_{60}$ heterojunctions with the cubic $MAPbI_3$ have the HOMO–LUMO gap of $MAPbI_3$ $E_g > 1.7$ eV and dissociation energy of the electron–hole pair $\Delta E > 0.8$ eV. In this case, the separation of photo-generated electron–hole pairs occurs at the interface, leading to a PCE of $\eta \sim 10\%$. The heterojunction with the tetragonal perovskites has a lower energy gap of $E_g < 1.7$ eV. However, the separation of photo-induced charge occurs only in the topC geometry with a PCE of $\eta > 14\%$ because this configuration has a low exciton dissociation energy of $\Delta E \leq 0.7$ eV,

Both the topN and apolar geometries have almost similar values of energy gap E_g and exciton dissociation energy ΔE. The electron-hole pair dissociation energy ΔE for the tetragonal $MAPbI_3$ with the topC orientation is $\sim$0.48–0.70 eV, which is lower than that of the topN and apolar geometries $\sim$ 0.84–0.98 eV. Compared with the topN or apolar case, the topC geometry has a higher energy gap of $E_g \sim 1.7$ eV and a smaller exciton dissociation energy of $\Delta E \sim 0.7$ eV. However, the topC case with C_{60} on the aboveI position is an exceptional case. It has the smallest exciton dissociation energy $\Delta E = 0.48$ eV and the smallest energy gap of $E_g = 1.41$ eV.

The heterojunction with the topC orientation exhibits a high PCE of $\eta > 14\%$. The PCE (η^*) values calculated using the three-fold degenerate LUMO of C_{60} fullerene are 1–3% higher than η (ESI†). Among the *t*-MAI slab models with the topC orientation, the highest PCE of $\eta \sim 18.7\%$ is realized when C_{60} is on the top of iodine or on the aboveI position. It has a higher efficiency of $\eta^* \sim 19.2\%$, if the three-fold degenerate LUMO of C_{60} is considered. On the other hand, the tetragonal-phase heterojunction with topN and apolar orientations does not yield nonzero PCE, implying that charge transfer does not occur at the $MAPbI_3$-C_{60} interface. Comparison to the heterojunction with tetragonal $MAPbI_3$, the cubic-phase heterojunction has a larger exciton dissociation energy of $\Delta E > 0.8$ eV and a higher energy gap of $E_g > 1.7$ eV, as summarized in Table S3 (ESI†). It is interesting to see that all the heterojunctions have a PCE of $\eta \geq 9\%$.

The interesting trends in the energy gap, the exciton dissociation energy, and the PCE in Fig. 6 can be understood by considering the effect of the surface electric dipole of $MAPbI_3$, originating from the organic MA cation, as shown in Fig. 2.

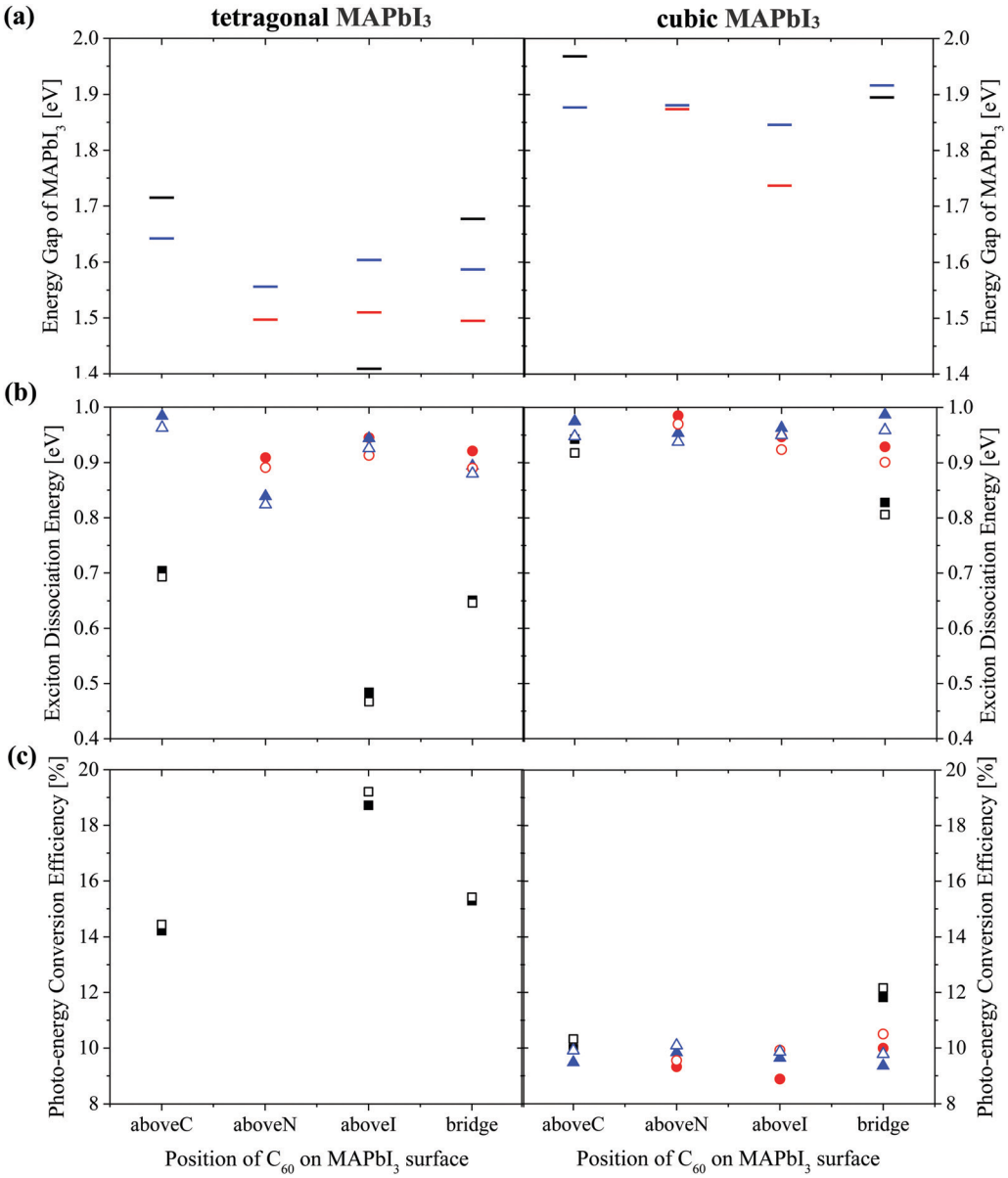

Fig. 6 (a) Energy gap of $MAPbI_3$ E_g (b) exciton dissociation energy and (c) photo-energy conversion efficiency of a $MAPbI_3/C_{60}$ heterojunction for different C_{60} adsorbed sites based on Tables S2 and S3 (ESI†). Orientations of the MA cation with respect to the (001) surface are: topC (black), topN (red) and apolar (blue). Open symbols (Fig. S8(b) and(c), ESI†) represent the results obtained by taking the average value of the three-fold degenerate LUMO of C_{60} fullerene.

This polar MA cation can rotate at room temperature and the positive charge is localized around the NH_3 group.[68] Therefore, the topC geometry with the CH_3 orienting towards the upper vacuum in all layers is favorable for the injection of photo-induced electrons into the LUMO of fullerene, as well as for the enhancement of the stability (as shown in Fig. 5(a)). The built-in electric field due to the inward pointing surface dipole of the MA cation of the topC geometry facilitates an oriented electron transport to fullerene and reduces charge recombination. For the particular case of the aboveI configuration, the separation of photogenerated electron–hole pairs is significantly enhanced by taking the advantage of electronegativity of iodine. Therefore, it has the lowest exciton dissociation energy of $\Delta E \sim 0.5$ eV and the highest PCE of $\eta \sim 19\%$. For the topN geometry, the outward pointing surface dipole leads to an internal field that reduces the stability of the $MAPbI_3/C_{60}$ heterojunction, as shown in Fig. 5(a). For the cubic $MAPbI_3$, one interesting feature, which can be seen from Fig. 6, is that the HOMO–LUMO gap of $MAPbI_3$ E_g, the exciton dissociation energy ΔE, and the PCE do not have an obvious dependence on the orientation of MAI and the location of C_{60} on the $MAPbI_3$ surface. This is attributed to the relatively weak polar behavior (and therefore, the built-in electric field) of the cubic $MAPbI_3$ as compared to the tetragonal phase.

In the present study, our predicted PCE values are comparable to the reported values of ~20% for the HTM-free PSC based on a $MAPbI_3$ with F4TCNQ molecules as the electron acceptor.[38] Cojocaru *et al.* studied the effect of temperature on the PCE of $MAPbI_3$ with both HTM and ETM layers.[69] They reported a PCE of $\eta \sim 14\%$ at temperature $T \sim 30$ °C, and the efficiency decreases to $\eta \sim 5\%$ at $T > 55$ °C. The performance decline of perovskite solar cells is also reported experimentally by Schwenzer *et al.*[70] Our calculations show that the tetragonal $MAPbI_3/C_{60}$ heterojunction with the C_{60} on the aboveC position of the topC $MAPbI_3$ surface has the highest PCE of $\eta \sim 19\%$, whereas the PCE of the heterojunction decreases to $\eta \sim 10\%$ for the case of a high-temperature cubic $MAPbI_3$. Since we consider only one C_{60} on a $MAPbI_3$ surface of 2×2 periodicity in-plane, the predicted PCE could be higher if a full coverage of C_{60} on the $MAPbI_3$ surface is performed. The present GGA-PBE calculation predicts bandgap values of $MAPbI_3$ surfaces that agree reasonably well with the experiments, as discussed earlier. This is due to the fortuitous cancellation of the GGA underestimated gap and the lack of the electron–hole coupling of exciton, which overestimates the optical gap.[66] Nevertheless, our calculated PCE values may not be accurate due to the use of GGA-PBE eigenvalues for E_g and ΔE, although they will give a rough estimation.

5 Conclusions

In summary, we have performed first-principles DFT calculations on the photo-energy conversion efficiency (PCE) of $MAPbI_3/C_{60}$ heterojunctions. Finite slab models of both tetragonal and cubic $MAPbI_3(001)$ surfaces with MAI terminations are considered. A fullerene C_{60} is introduced to different positions of the $MAPbI_3$ surface. Our studies reveal that the stability, the exciton dissociation efficiency, and the PCE of the heterojunction with the tetragonal $MAPbI_3$ strongly depend on the nature of the $MAPbI_3$ surfaces. The $MAPbI_3/C_{60}$ heterojunction with CH_3 of the MA cation orienting towards the upper vacuum in all layers is energetically more stable than the $MAPbI_3$ with the CH_3 orienting towards the upper vacuum in all layers (the topN geometry), or the $MAPbI_3$ with half of the MA cations having their $-NH_3$ or $-CH_3$ groups pointing up (and half pointing down) (the apolar geometry). In this case, the built-in field forms from the inward pointing the surface electric dipole of the MA cations of the topC geometry promoting the electron transfer to fullerene and suppressing charge recombination, implying an electric–dipole aided charge separation. The recent experimental observations of the enhancement of PCE in the $MAPbI_3$ solar cells by coupling the perovskites with ferroelectrics or by applying an electrical poling further support the importance of this phenomenon.[71,72] Recently, Yu *et al.* studied the effect of Lewis base and graphene on the performance of MAPbI3 solar cells.[73] Their study demonstrates the important role of the interface dipole in the improved performance of PSCs by facilitating the electron extraction *via* graphene. The separation of photogenerated electron–hole pairs is further enhanced when C_{60} is located directly on the top of iodine. We find that the functionalization of topC-$MAPbI_3$ with a fullerene can achieve a high PCE of $\eta > 14\%$, and the highest efficiency of $\eta \sim 19\%$ can be achieved when the fullerene is located directly on the top of iodine. However, a drawback is that this heterojunction can harvest light and convert to energy only if the fullerene (or an electron transport material) is located on $MAPbI_3$ with the topC geometry, but not the topN or apolar geometry. A fullerene absorbed on a cubic $MAPbI_3$ surface gives a lower PCE of $\eta \sim 10\%$, although the stability and PCE do not sensitively depend on the MA orientation and the C_{60} position on the $MAPbI_3$ surface.

Conflicts of interest

There are no conflicts of interest to declare.

Acknowledgements

This work has been supported by the Institute for Materials Research (IMR), Tohoku University and Dassault Systèmes BIOVIA for the use of supercomputer facilities of IMR and for the ambassador license of BIOVIA. KHChew acknowledges the support from the Air Force Office of Scientific Research under award number FA2386-20-1-4011.

References

1 A. K. Jena, A. Kulkarmi and T. Miyasaka, *Chem. Rev.*, 2019, **119**, 3036–3103.
2 A. Kojima, K. Teshima, Y. Shirai and T. Miyasaka, *J. Am. Chem. Soc.*, 2009, **131**, 6050–6051.
3 M. M. Lee, J. Teuscher, T. Miyasaka, T. N. Murakami and H. J. Snaith, *Science*, 2012, **338**, 643–647.
4 W. S. Yang, J. H. Noh, N. J. Jeon, Y. C. Kim, S. Ryu, J. Seo and S. I. Seok, *Science*, 2015, **348**, 1234–1237.
5 M. A. Green, E. D. Dunlop, J. Hohl-Ebinger, M. Yoshita, N. Kopidakis and X. Hao, *Prog. Photovoltaics*, 2020, **28**, 629–638.
6 S. Chen, Y. Hou, H. Chen, M. Richter, F. Guo, S. Kahmann, X. Tang, T. Stubhan, H. Zhang, N. Li, N. Gasparini, C. O. R. Quiroz, L. S. Khanzada, G. J. Matt, A. Osvet and C. J. Brabec, *Adv. Energy Mater*, 2016, **6**, 1600132.
7 W. Yang, Y. Yao and C.-Q. Wu, *J. Appl. Phys.*, 2015, **117**, 095502.
8 Y. Zhou and A. A. Gray-Weale, *Phys. Chem. Chem. Phys.*, 2016, **18**, 4476–4486.
9 Y. Zhou and G. Long, *J. Phys. Chem. C*, 2017, **121**, 1455–1462.
10 A. Poglitsch and D. Weber, *J. Chem. Phys.*, 1987, **87**, 6373–6378.
11 H. Gaonkar, J. Zhu, R. Kottokkaran, B. Bhageri, M. Noack and V. Dalal, *ACS Appl. Energy Mater.*, 2020, **3**, 3497–3503.
12 G. Yu, J. Gao, J. C. Hummelen, F. Wudi and A. J. Heeger, *Science*, 1995, **270**, 1789.
13 P. Peumans, A. Yakimov and S. R. Forrest, *J. Appl. Phys.*, 2003, **93**, 3693.

14 J. Drechsel, B. Männig, F. Kozlowski, M. Pfeiffer and K. Leo, *Appl. Phys. Lett.*, 2005, **86**, 244102.
15 Y. Kodama and K. Ohno, *Appl. Phys. Lett.*, 2010, **96**, 034101.
16 S. Ono, R. Kuwahara and K. Ohno, *J. Appl. Phys.*, 2014, **116**, 054305.
17 Y. Fang, C. Bi, D. Wang and J. Huang, *ACS Energy Lett.*, 2017, **2**, 782–794.
18 T. Gatti, E. Menna, M. Meneghetti, M. Maggini, A. Petrozza and F. Lamberti, *Nano Energy*, 2017, **41**, 84–100.
19 J. Pascual, J. L. Delgado and R. Tena-Zaera, *J. Phys. Chem. Lett.*, 2018, **9**, 2893–2902.
20 E. Castro, J. Murillo, O. Fernandez-Delgado and L. Echegoyen, *J. Mater. Chem. C*, 2018, **6**, 2635–2651.
21 Y. Shao, Z. Xiao, C. Bi, Y. Yuan and J. Huang, *Nat. Commun.*, 2014, **5**, 5784.
22 J. Xu, A. Buin, A. H. Ip, W. Li, O. Voznyy, R. Comin, M. Yuan, S. Jeon, Z. Ning, J. J. McDowell, P. Kanjanaboos, J. P. Sun, X. Lan, L. N. Quan, D. H. Kim, I. G. Hill, P. Maksymovych and E. H. Sargent, *Nat. Commun.*, 2015, **6**, 7081.
23 J.-Y. Jeng, Y.-F. Chiang, M.-H. Lee, S.-R. Peng, T.-F. Guo, P. Chen and T.-C. Wen, *Adv. Mater.*, 2013, **25**, 3727–3732.
24 X. Zheng, B. Chen, J. Dai, Y. Fang, Y. Bai, Y. Lin, H. Wei, X. C. Zeng and J. Huang, *Nat. Energy*, 2017, **2**, 17102.
25 H. Rao, S. Ye, W. Sun, W. Yan, Y. Li, H. Peng, Z. Liu, Z. Bian, Y. Li and C. A. Huang, *Nano Energy*, 2016, **27**, 51–57.
26 H. Yoon, S. M. Kang, J.-K. Lee and M. Choi, *Energy Environ. Sci.*, 2016, **9**, 2262–2266.
27 K.-M. Lee, C.-C. Chen, L.-C. Chen, S. H. Chang, K.-S. Chen, S.-C. Yeh, C.-T. Chen and C.-G. Wu, *Sol. Energy Mater. Sol. Cells*, 2017, **164**, 13–18.
28 D. Liu, Q. Wang, C. J. Traverse, C. Yang, M. Young, P. S. Kuttipillai, S. Y. Lunt, T. W. Hamann and R. R. Lunt, *ACS Nano*, 2018, **12**, 876–883.
29 Z. Song, A. Abate, S. C. Watthage, G. K. Liyanage, A. B. Phillips, U. Steiner, M. Graetzel and M. J. Heben, *Adv. Energy Mater.*, 2016, **6**, 1600846.
30 Y. Han, S. Meyer, Y. Dkhissi, K. Weber, J. M. Pringle, U. Bach, L. Spiccia and Y.-B. Cheng, *J. Mater. Chem. A*, 2015, **3**, 8139–8147.
31 M. I. Saidaminov, J. Kim, A. Jain, R. Quintero-Bermudez, H. Tan, G. Long, F. Tan, A. Johnston, Y. Zhao, O. Voznyy and E. H. Sargent, *Nat. Energy*, 2018, **3**, 648–654.
32 H. S. Kim, C. R. Lee, J. H. Im, K. B. Lee, T. Moehl, A. Marchioro, S.-J. Moon, H.-B. Robin, J.-H. Yum, J. E. Moser, M. Grätzel and N.-G. Park, *Sci. Rep.*, 2012, **2**, 591.
33 R. S. Sanchez and E. Mas-Marza, *Sol. Energy Mater. Sol. Cells*, 2016, **158**, 189–194.
34 K. Domanski, J.-P. Correa-Baena, N. Mine, M. K. Nazeeruddin, A. Abate, M. Saliba, W. Tress, A. Hagfeldt and M. Grätzel, *ACS Nano*, 2016, **10**, 6306–6314.
35 A. K. Jena, Y. Numata, M. Ikegami and T. Miyasaka, *J. Mater. Chem. A*, 2018, **6**, 2219–2230.
36 L. Etgar, P. Gao, Z. Xue, Q. Peng, A. K. Chandiran, B. Liu, M. K. Nazeeruddin and M. Grätzel, *J. Am. Chem. Soc.*, 2012, **134**, 17396–17399.
37 H. Chen and S. Yang, *Adv. Mater.*, 2017, **29**, 1603994.
38 W.-Q. Wu, Q. Wang, Y. Fang, Y. Shao, S. Tang, Y. Deng, H. Lu, Y. Liu, T. Li, Z. Yang, A. Gruverman and J. Huang, *Nat. Commun.*, 2018, **9**, 1625.
39 S. Yun, X. Zhou, J. Even and A. Hagfeldt, *Angew. Chem., Int. Ed.*, 2017, **56**, 15806–15817.
40 X. Zhou, J. Jankowska, H. Dong and O. V. Prezhdo, *J. Energy Chem.*, 2018, **27**, 637–649.
41 C.-J. Yu, *J. Phys. Energy*, 2019, **1**, 022001.
42 J. Yin, D. Cortecchia, A. Krishna, S. Chen, N. Mathews, A. C. Grimsdale and C. Soci, *J. Phys. Chem. Lett.*, 2015, **6**, 1396–1402.
43 C. Quarti, F. D. Angelis and D. Beljonne, *Chem. Mater.*, 2017, **29**, 958–968.
44 W. Shockley and H. J. Queisser, *J. Appl. Phys.*, 1961, **32**, 510.
45 K. Seki, A. Furube and Y. Yoshida, *Appl. Phys. Lett.*, 2013, **103**, 253904.
46 M. I. Hossain, W. Qarony, S. Ma, L. Zeng, D. Knipp and Y. H. Tsang, *Nano-Micro Lett.*, 2019, **11**, 58.
47 Refer https://rredc.nrel.gov/solar//spectra/am1.5/for Reference Solar Spectral Irradiance: Air Mass 1.5.
48 B. Delley, *J. Chem. Phys.*, 1990, **92**, 508–517.
49 B. Delley, *J. Chem. Phys.*, 2000, **113**, 7756–7764.
50 B. Delley, *Modern Density Functional Theory: A Tool for Chemistry in Theoretical and Computational Chemistry*, Elservier, ed. J. M. Seminario and P. Politzer, 1995, vol. 2.
51 E. R. McNellis, J. Meyer and K. Reuter, *Phys. Rev. B: Condens. Matter Mater. Phys.*, 2009, **80**, 205414.
52 A. Tkatchenko and M. Scheffler, *Phys. Rev. Lett.*, 2009, **102**, 073005.
53 C. Motta, F. El-Mellouhi, S. Kais, N. Tabet, F. Alharbi and S. Sanvito, *Nat. Commun.*, 2015, **6**, 7026.
54 J. P. Perdew, K. Burke and M. Ernzerhof, *Phys. Rev. Lett.*, 1996, **77**, 3865–3868.
55 W.-J. Yin, T. Shi and Y. Yan, *J. Phys. Chem. C*, 2015, **119**, 5253–5264.
56 R. A. Jishi, O. B. Ta and A. A. Sharif, *J. Phys. Chem. C*, 2014, **118**, 28344–28349.
57 W. Geng, L. Zhang, Y.-N. Zhang, W.-M. Lau and L.-M. Liu, *J. Phys. Chem. C*, 2014, **118**, 19565–19571.
58 A. M. A. Leguy, J. M. Frost, A. P. McMahon, V. G. Sakai, W. Kockelmann, C. Law, X. Li, F. Foglia, A. Walsh, B. C. O'Regan, J. Nelson, J. T. Cabral and P. R. F. Barnes, *Nat. Commun.*, 2015, **6**, 7124.
59 T. Baikie, N. S. Barrow, Y. Fang, P. J. Keenan, P. R. Slater, R. O. Piltz, M. Gutmann, S. G. Mhaisalkar and T. J. White, *J. Mater. Chem. A*, 2015, **3**, 9298–9307.
60 Y. Kawamura, H. Mashiyama and K. Hasebe, *J. Phys. Soc. Jpn.*, 2002, **71**, 1694–1697.
61 W.-J. Yin, J.-H. Yang, J. Kang, Y. Yan and S.-H. Wei, *J. Mater. Chem. A*, 2015, **3**, 8926–8942.
62 F. Brivio, K. T. Butlet, A. Walsh and M. Van Schilfgaarde, *Phys. Rev. B: Condens. Matter Mater. Phys.*, 2014, **89**, 155204.
63 T. Ahmed, C. La-O-Varakiat, T. Salim, Y. M. Lam, E. E. M. Chia and J.-X. Zhu, *EPL*, 2014, **108**, 67015.
64 Y. Yamada, T. Nakamura, M. Endo, A. Wakamiya and Y. Kanemitsu, *Appl. Phys. Express*, 2014, **7**, 032302.

65 V. D'Innocenzo, G. Grancini, M. J. P. Alcocer, A. R. S. Kandada, S. D. Stranks, M. M. Lee, G. Lanzani, H. J. Snaith and A. Petrozza, *Nat. Commun.*, 2014, **5**, 3586.
66 E. Mosconi, A. Amat, M. K. Nazeeruddin, M. Grätzel and F. D. Angelis, *J. Phys. Chem. C*, 2013, **117**, 13902–13913.
67 Y. Inada and H. Orita, *J. Comput. Chem.*, 2008, **29**, 225–232.
68 A. Stroppa, C. Quarti, F. D. Angelis and S. Picozzi, *J. Phys. Chem. Lett.*, 2015, **6**, 2223–2231.
69 L. Cojocaru, S. Uchida, Y. Sanehira, V. Gonzalez-Pedro, J. Bisquert, J. Nakazaki, T. Kubo and H. Segawa, *Chem. Lett.*, 2015, **44**, 1750–1752.
70 J. A. Schwenzer, L. Rakocevic, R. Gehlhaar, T. Abzieher, S. Gharibzadeh, S. Maghadamzadeh, A. Quintilla, B. S. Richards, U. Lemmer and U. W. Paetzold, *ACS Appl. Mater. Interfaces*, 2018, **10**, 16390–16399.
71 E. Jia, D. Wei, P. Cui, J. Ji, H. Huang, H. Jiang, S. Dou, M. Li, C. Zhou and W. Wang, *Adv. Sci.*, 2019, **6**, 1900252.
72 A. Bruno, D. Cortecchia, X. Y. Chin, K. Fu, P. P. Boix, S. Mhaisalkar and C. Soci, *Adv. Energy Mater.*, 2017, 1700265.
73 C.-J. Yu, Y.-H. Kye, U.-G. Jong, K.-C. Ri, S.-H. Choe, J.-S. Kim, S.-G. Ko, G.-I. Ryu and B. Kim, *ACS Appl. Mater. Interfaces*, 2020, **12**, 1858–1866.